Journal of *Marine Science and Engineering*

MDPI

Article

Numerical Simulations of Seaplane Ditching on Calm Water and Uniform Water Current Coupled with Wind

Ruosi Zha [1], Kai Wang [1,*], Jianglong Sun [2,3], Haiwen Tu [4] and Qi Hu [5]

[1] School of Ocean Engineering and Technology, Sun Yat-sen University & Southern Marine Science and Engineering Guangdong Laboratory (Zhuhai), Zhuhai 519082, China; zhars@mail.sysu.edu.cn
[2] School of Naval Architecture and Ocean Engineering, Huazhong University of Science and Technology, Wuhan 430074, China; sundapao@hust.edu.cn
[3] Hubei Provincial Engineering Research Center of Data Techniques and Supporting Software for Ships (DTSSS), Wuhan 430074, China
[4] College of Marine Science and Technology, China University of Geosciences, Wuhan 430074, China; tuhw@cug.edu.cn
[5] Key Laboratory of High-Speed Hydrodynamic Aviation Science and Technology, China Special Vehicle Research Institute, Jingmen 448035, China; huq005@avic.com
* Correspondence: wangkai25@mail.sysu.edu.cn

Abstract: In this paper, the ditching performance of a seaplane model on calm water and a uniform water current coupled with wind was numerically investigated. The overset grid technique was applied to treat the large amplitude of the body motions of the seaplane without leading to mesh distortion. The effects of the initial velocity and the initial pitch angle on the slamming loads and motion responses were investigated for the seaplane's ditching on calm water. A good agreement with the experimental data on the velocity and angle was obtained. Besides ditching on calm water without the water current and wind, three more-complicated conditions were adopted, including the seaplane's ditching on calm water with wind, a water current without wind, and a water current coupled with wind. The accelerations and impact pressures of the seaplane can be influenced by the wind or current. Water splashing and overwashing could be observed during the water entry process, with water overtopping the seaplane head or nose and flowing over the body surface. It can be concluded that the relative motion between the water and the seaplane model should be carefully controlled to avoid possible damages caused by the occurrence of overwashing.

Keywords: seaplane; ditching; slamming; overwash; overset

check for updates

Citation: Zha, R.; Wang, K.; Sun, J.; Tu, H.; Hu, Q. Numerical Simulations of Seaplane Ditching on Calm Water and Uniform Water Current Coupled with Wind. *J. Mar. Sci. Eng.* **2024**, *12*, 296. https://doi.org/10.3390/jmse12020296

Academic Editors: Young-Bok Kim and Nam-kyun Im

Received: 9 January 2024
Revised: 31 January 2024
Accepted: 4 February 2024
Published: 7 February 2024

Copyright: © 2024 by the authors. Licensee MDPI, Basel, Switzerland. This article is an open access article distributed under the terms and conditions of the Creative Commons Attribution (CC BY) license (https://creativecommons.org/licenses/by/4.0/).

1. Introduction

A seaplane landing on water, which is known as ditching [1], is of great importance for the operating performance and structural safety due to the instantaneous huge slamming loads. During the ditching process, a plane is subjected to both hydrodynamic and aerodynamic loads and, therefore, complicated body motions with translations and rotations can be generated. The vertical loads and pitch angle are of concern for plane ditching under various conditions, especially the water current and wind. It is necessary to adjust the plane attitude to mitigate or avoid impact damages during ditching on water. Lou et al. [2] studied the flight performance of a preliminarily designed solar-powered unmanned seaplane and discussed the parameter effects, such as the wing loading, takeoff time, weight, cruise speed, takeoff ground distance, takeoff ground time, flight envelope, and endurance.

The ditching process of a seaplane can usually be simplified as a typical water entry problem, which was pioneered by von Karman in 1929 [3]. Most of the analytical methods were based on the assumption of shallow body submergence and limited to simple geometries. The water entry of a two-dimensional seaplane model was theoretically analyzed, and the water loads during ditching were predicted based on the change of the added mass.

The effects of the free surface were neglected. Wanger [4] improved the analytical solutions by considering the free surface and water splash. The second-order Wagner's theory was further improved for solving water entry problems at small deadrise angles using a systematic matched asymptotic analysis by Oliver [5]. Recently, Chatjigeorgiou [6] proposed an analytical approach based on asymptotic analysis using both the von Karman [3] and the Wagner [4] models of water impact to study the slamming of a three-dimensional elliptic paraboloid.

Experiments on the water entry problems have also been widely conducted to study the slamming-induced loads and motions. For example, a wedge can be regarded as the section of an aircraft. A series of water entry tests of a wedge section at the Norwegian Marine Technology Research Institute (MARINTEK) was conducted by Zhao et al. [7]. Jet flows were observed, and the experimental data were compared with the theoretical solutions for validation. Barjasteh et al. [8] experimentally investigated the wedges with different tilt angles, deadrise angles, and impact speeds entering the water. The results indicated that even a small inclination angle can lead to pretty high pressures with a small deadrise angle. The acceleration characteristics of both the wedge and arc body models free falling on the water were investigated by model tests, which were conducted by Zhang et al. [9]. It was found that the air bubble in the cavity could impact the peak accelerations. Iafrati and Grizzi [10] tested the ditching of a fuselage during an emergency landing on water and studied the flow modalities of cavitation and ventilation. The relations between the transition from the cavitation to the ventilation condition and the dynamic responses of the fuselage were analyzed. A vertical ditching test was designed and conducted by Nicolosi et al. [11], and the peak pressures and accelerations were measured with different dropping heights/speeds. Experimental tests are the most-reliable methods, which, however, have the high costs of model manufacturing, tank facilities, and labor.

Computational fluid dynamics (CFD) methods have been developed over the years and have been applied to solve the water entry problems and simulate the ditching of a seaplane. The cost of CFD simulations is less than conducting experimental tests. Highly nonlinear multiphase problems are addressed by many CFD approaches including mesh-based, mesh-free, and hybrid methods. The volume of fluid (VOF) method was employed to capture the interfaces between two fluid phases in the numerical simulations of slamming by Schellin and El Moctar [12]. One of the main challenges for simulations of seaplane ditching on water is the treatment of the large amplitude of the plane's body motions. A global moving mesh method was adopted by Qu et al. [13] to overcome the large deformation of the mesh by using traditional dynamic mesh methods. The water impact loads and motions of the plane during the ditching process were numerically validated and analyzed. Qu et al. [14] also studied the ditching performance of a regional aircraft by solving the Reynolds-averaged Navier–Stokes (RANS) equations based on the finite-volume method (FVM). In this work, it was concluded that the water landing safety can be improved by setting a large initial pitch angle. Recently, Qu et al. [15] used the coupled Euler Lagrangian method to study the load characteristics of a Twin-Float seaplane when it was landing in waves with different wave heights. Bouncing phenomena were observed when the seaplane landed on the wave. Zheng et al. [16] studied the motion of porpoising and the stability of a blended wing body plane ditching on water, which can be caused by a higher initial speed or pitch angle before slamming. The performance of a fixed-wing multi-rotor Unmanned Aerial Vehicle (UAV) with different control parameters was parametrically studied by Benmoussa and Gamboa [17]. Song et al. [18] studied the suction force, pressure, free surface, and motion of a seaplane model by using the overset mesh method, and the coupled hydrodynamic and aerodynamic effects were comprehensively analyzed. Compared with the mesh-based CFD methods, meshfree methods including the Lagrangian particle methods have advantages in simulating highly deformed free surfaces or interfaces. For example, Xiao et al. [19] developed a smoothed particle hydrodynamics (SPH) method and applied it to study a helicopter without wings ditching on water. The SPH method was also adopted by Woodgate et al. [20] to study helicopter fuselage

ditching in various sea states. A study of the comparisons between mesh-based and particle-based CFD methods was carried out by Xu et al. [21] by simulating seaplane ditching with splashing waves. Good agreement was achieved, and the SPH method was concluded to be superior in treating the water splashing in high-speed taxiing.

However, most experimental and numerical studies on plane ditching focus on calm water. Plane ditching on water with coupled current and wind is very limited. In this paper, mesh-based CFD methods based on FVM discretization and the overset grid technique were applied to numerically investigate a plane model ditching on water with current and wind. The VOF method was made advantage of to capture the water–air interface and simulate the phenomenon of overwashing. The numerical results for different initial velocities and initial pitch angles of the plane were compared. For verification, spatial and temporal convergence studies were carried out using three sets of refined meshes and three time steps, respectively. The final results were compared with the experimental data obtained by Mcbride and Fisher [22]. In spite of the ditching on calm water, a series of cases with various combinations of wind and current were studied to investigate the effects of water current and wind on the ditching motion and loads.

A flow chart of the present study summarizing the main steps and methods can be found in Figure 1. This paper is organized as follows. Section 1 presents an introduction to the phenomenon of a seaplane ditching on water and the latest studies of the ditching performance using various research methods, which is followed by the mathematical models and numerical methods in Section 2. Section 3 describes the geometry of the plane model, the computational domain with the boundary conditions, and the grid generation. Section 4 gives the results of the verification and validation and, then, the numerical analysis of the plane ditching on calm water under different operating conditions. The main conclusions in this study are drawn and summarized in Section 5.

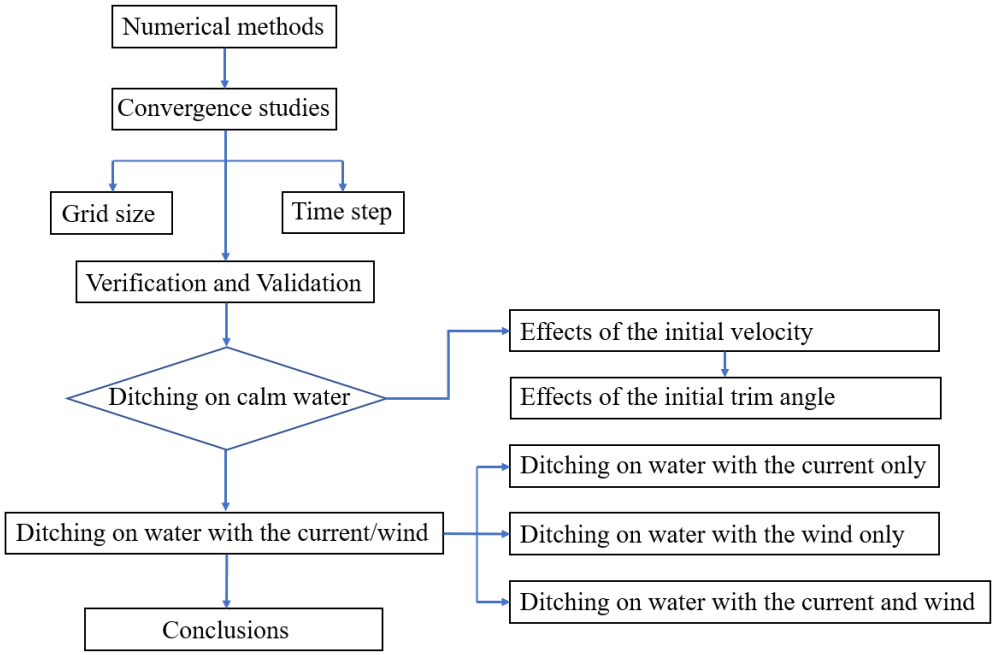


Figure 1. A flow chart of the present study.

2. Numerical Methods

2.1. Governing Equations

Water flow can be regarded as incompressible at normal temperature and pressure. Note that, in the cases with low Mach numbers, typically less than 0.3, the compressibility of air can also be neglected. The Reynolds-averaged Navier–Stokes (RANS) equations are

taken for the governing equations for the incompressible viscous flow. These equations can be expressed as follows, which consist of the continuity equation and momentum equation.

$$\frac{\partial u_i}{\partial x_i} = 0 \tag{1}$$

$$\rho\frac{\partial u_i}{\partial t} + \rho u_j\frac{\partial u_i}{\partial x_j} = -\frac{\partial p}{\partial x_i} + \frac{\partial}{\partial x_j}\left[\mu\left(\frac{\partial u_i}{\partial x_j} + \frac{\partial u_j}{\partial x_i}\right)\right] + \frac{\partial}{\partial x_j}(-\rho\overline{u_i'u_j'}) \tag{2}$$

where u_i, ρ, p, μ, and $-\rho\overline{u_i'u_j'}$ ($i = 1,\ 2$ and 3) denote the velocity components along the x-, y-, and z-axis, the pressure of the fluid, the density of the fluid, the dynamic viscosity of the fluid, and the term of Reynolds stresses [23]. Turbulence models are introduced to solve the Reynolds stresses. Two phases of fluid were simulated in the present simulations, and the VOF method was applied to capture the free surface between the water and air.

2.2. Turbulence Modeling

One of the most-prevalent methods to solve the Reynolds stresses is using eddy viscosity turbulence models based on the Boussinesq hypothesis. Based on the eddy viscosity models, the Reynolds stresses can be calculated by:

$$-\rho\overline{u_i'u_j'} = \mu_t\left(\frac{\partial u_i}{\partial x_j} + \frac{\partial u_j}{\partial x_i}\right) - \frac{2}{3}\rho k\delta_{ij} \tag{3}$$

where μ_t and δ_{ij} are the eddy viscosity and the Kronecker delta, respectively. $k = \frac{1}{2}\overline{u_i'u_j'}$ stands for the turbulent kinetic energy. The Spalart–Allmaras (SA) model [24] is an instance of the one-equation eddy viscosity model. The SA model solves a transport equation to calculate the modified diffusivity, $\tilde{\nu}$, which is used to determine the turbulence eddy viscosity, μ_t. The SA model exhibits excellent convergence and robustness for specific flows. Nevertheless, the dimensions and durations of the turbulence are not as distinctly established. This paper utilized two-equation eddy viscosity models to calculate the Reynolds stresses in the RANS equations. These models include solving independent transport equations for both the velocity and length scale. The turbulence length scale is determined by calculating the ratio of the kinetic energy to the dissipation rate. Commonly used turbulence models comprise the conventional k-ε model, the conventional k-ω model [25], the Shear Stress Transport (SST) k-ω models [26], etc. In the standard k-ε model, the turbulent eddy viscosity is calculated as:

$$\mu_t = \rho C_\mu f_\mu kT \tag{4}$$

where C_μ is a model coefficient, f_μ is a damping function, and T is the turbulent time scale calculated by:

$$T = \max(T_e, C_t\sqrt{\frac{\nu}{\varepsilon}}) \tag{5}$$

where $T_e = \frac{k}{\varepsilon}$ is the large-eddy time scale. C_t, ν, k, and ε are a model coefficient, the kinematic viscosity, the turbulent kinetic energy, and the turbulence dissipation rate, respectively. The transport equations for k and ε are written as:

$$\begin{aligned}\frac{\partial}{\partial t}(\rho k) + \nabla\cdot(\rho k\bar{\mathbf{v}}) =& \nabla\cdot\left[(\mu + \frac{\mu_t}{\sigma_k})\nabla k\right] + P_k + S_k \\ & - \rho(\varepsilon - \varepsilon_0)\end{aligned} \tag{6}$$

$$\begin{aligned}\frac{\partial}{\partial t}(\rho\varepsilon) + \nabla\cdot(\rho\varepsilon\bar{\mathbf{v}}) =& \nabla\cdot\left[(\mu + \frac{\mu_t}{\sigma_\varepsilon})\nabla\varepsilon\right] + \frac{1}{T_e}C_{\varepsilon1}P_\varepsilon \\ & - C_{\varepsilon2}f_2\rho(\frac{\varepsilon}{T_e} - \frac{\varepsilon_0}{T_0}) + S_\varepsilon\end{aligned} \tag{7}$$

where σ_k, σ_ε, $C_{\varepsilon 1}$, and $C_{\varepsilon 2}$ are the model coefficients, P_k and P_ε are the production terms, f_2 is a damping function, and S_k and S_ε are the source terms.

In contrast to the conventional k-ε model, the realizable k-ε model solves the turbulent eddy viscosity by treating C_μ as a variable instead of a constant [27]. The dissipation rate transportation has been rephrased. The realizable k-ε model is more effective in accurately representing the average flow of intricate structures and in simulating flows that involve rotation. The current simulations utilized the realizable k-ε two-layer model [27] with an all-y^+ wall treatment [28].

2.3. Finite-Volume Discretization

The finite-volume method [29] was applied in this paper for discretizing the partial differential equations. The body-fitted mesh technology is used to treat complicated geometries, e.g., a plane with wings and an empennage. The discretized convective term at the face of a mesh cell can be written as:

$$(\phi\rho\mathbf{v}\cdot\mathbf{a})_f = (\dot{m}\phi)_f = \dot{m}_f\phi_f \tag{8}$$

where ϕ_f and $\dot{m}_f$ denote an arbitrary fluid property and the mass flow rate at the face of a grid cell, respectively. The convective flux can be calculated by employing the second-order upwind (SOU) scheme as Equation (9). The diffusive flux through the internal cell faces of a grid cell is discretized as Equation (10).

$$(\dot{m}\phi)_f = \begin{cases} \phi_0 + (x_f - x_0)\cdot(\nabla\phi)_{r,0} & for\ \dot{m}_f \geq 0 \\ \phi_1 + (x_f - x_1)\cdot(\nabla\phi)_{r,1} & for\ \dot{m}_f < 0 \end{cases} \tag{9}$$

$$D_f = (\Gamma\nabla\phi\cdot\mathbf{a})_f \tag{10}$$

where Γ stands for the face diffusivity.

2.4. Overset Grid Technique

The overset grid technique [30] is utilized to deal with the body movements exhibited by the seaplane. The commercial CFD software, STAR-CCM+ 17.04.008-R8 , has the overset capability, which allows for the simulation of complex moving geometries. By applying the overset grid technique, multiple overlapping grids can be generated and move independently of each other. Individual grids are created firstly, e.g., the statical background grids for the computational domain and the overset grids for the domain covering the moving geometry. They can be then combined into a total mesh by defining the overlapping region, which is called the overset interface, between the static background grids and the overset grids. After the overset mesh is generated, the hole-cutting procedure can automatically connect the overset region with the background region via the overset interface. The data transfer through the overset interface is implicitly coupled, meaning that a solution is calculated on all grids at the same time, resulting in enhanced robustness and convergence. Triangular or tetrahedral interpolation elements are employed for 2D and 3D simulations, respectively. The commonly used interpolation algorithms include the distance-weighted, linear, linear quasi-2D, or least-squares interpolations.

It is also needed to specify how the grids move relative to each other according to the movement of the wall boundary of the solid body. The Dynamic Fluid–Body Interaction (DFBI) model [31] allows for the solution of body motions in case mobility is not predetermined. The object's movement, resulting from the influence of fluids and other forces, is transmitted via the overset mesh. The DFBI contact coupling model enables bodies to collide and bounce from touch by simulating a repulsive force. The geometry can move arbitrarily inside the background mesh without leading to mesh distortions and collapses.

2.5. Six-Degree-of-Freedom Body Motions

The motion of a ditching plane is governed by the equations of the rigid body dynamics, following Newton's law of motion. The free movement of a solid body includes the coupling of translation and rotation along the X-, Y-, and Z-axis directions, i.e., the surge, sway, heave, roll, pitch, and yaw. The Earth-fixed and body-fixed coordinate systems are adopted to solve the six-degree-of-freedom (six-DoF) equations of motion. To solve the six-DoF equations of a rigid body, the total force on the body and moment based on the mass center of the body are firstly calculated in the Earth-fixed coordinate system:

$$\boldsymbol{F_e} = (X_e, Y_e, Z_e) = mg + \int (\tau d|S_e| + pdS_e) \tag{11}$$

$$\boldsymbol{M_e} = (K_e, M_e, N_e) = r_{cg} \times mg + \int r \times (\tau d|S_e| + pdS_e) \tag{12}$$

where $\boldsymbol{F_e}$ and $\boldsymbol{M_e}$ are the total force and moment exerted on the rigid body in the Earth-fixed coordinate system, respectively. τ and p are the shear force and the total pressure on the body surface. S_e is the normal vector of the particle on the body surface. Note that the velocities should be solved in the body-fixed coordinate system and, then, transferred to the Earth-fixed coordinate system. Finally, the solid body will be moved according to its velocity and displacement in the Earth-fixed coordinate system.

3. Model and Grid Generation

3.1. Geometry of the Model

Numerical simulations were carried out for the model of the National Advisory Committee for Aeronautics (NACA) TN2929 plane (Model A) [22], which is widely used for investigating the phenomenon of a plane ditching on water. Different views of the plane geometry are shown in Figure 2, including the front view (A), the lateral view (B), and the upward view (C). It can be seen that the TN2929 model is composed of a slender spindle-like fuselage, two wings, and an empennage. Note that the fuselage will impact the water surface while the seaplane is landing on the water. The main particulars of the present geometry are listed in Table 1. It should be noted that the fitness ratio of the present model is 6. The width of the wings is 1.6764 m, while the width of the fuselage is 0.29845 m. A half model was used for the present simulations, and the values of the mass and the moment of inertia were half of the values listed in Table 1.

Table 1. Main particulars of the NACA TN2929 model.

Items	Symbol	Value
Length	L (m)	1.2192
Width	B (m)	1.6764
Height	h (m)	0.2985
Mass	m (kg)	5.6750
Area of wings	S (m^2)	0.4045
Center of gravity	COG_x (m)	0.5705
Center of gravity	COG_z (m)	0.1015
Moment of inertia	I_{xx} ($kg{\cdot}m^2$)	0.29245
Moment of inertia	I_{yy} ($kg{\cdot}m^2$)	0.29245

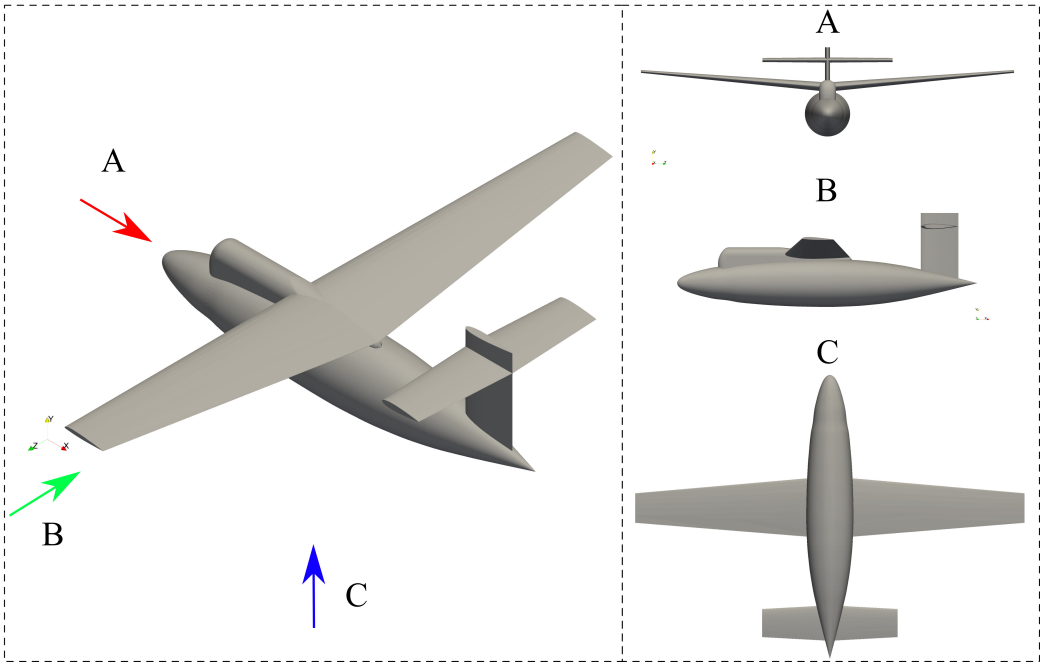


Figure 2. NACA TN2929 plane model with (**A**) the front view, (**B**) the lateral view, and (**C**) the upward view.

3.2. Computational Domain

As shown in Figure 3, a cuboid domain was applied in the present numerical simulations, whose length, width, and height were 12L, 3L, and 5L, respectively. The origin of the Earth-fixed coordinate system was set on the free surface, with a water depth of 3L. Initially, the distance between the seaplane model and the outlet boundary was 2L. The plane then ditched on water and moved toward the negative x-axis direction. The boundary conditions are also given in Figure 3. A no-slip moving wall boundary condition was imposed on the surface of the seaplane model. A symmetry plane boundary condition was used to save computational cost, in which only a half-seaplane model can be considered by taking advantage of the symmetrical structure of the seaplane model about the plane $y = 0$ m. Besides the symmetry plane and the pressure outlet, other boundaries were set as the velocity inlet. For the cases of ditching on calm water, the uniform velocity at the inlet was zero. The reference pressure was specified as zero at the outlet boundary, which means the relative pressure of one standard atmospheric pressure. The wind direction and the current direction were both set along the x-axis. The relative angle between the wind/current and the advancing seaplane model was then 180 degrees.

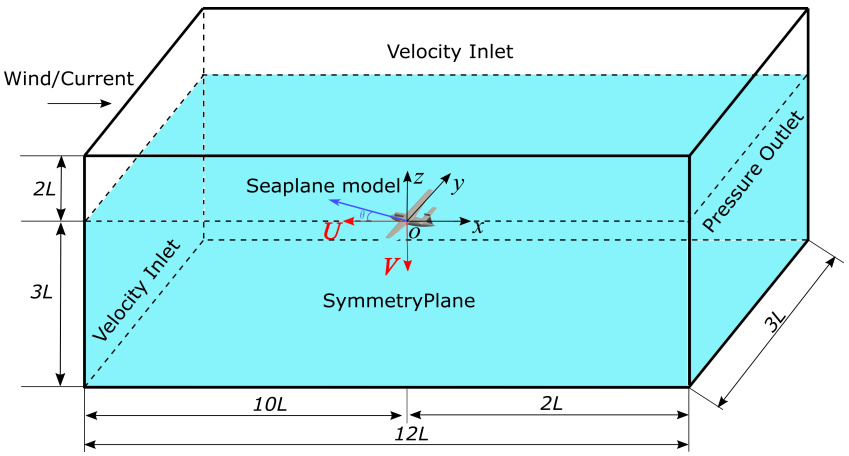


Figure 3. The computational domain and definitions of the coordinate systems and boundary conditions.

3.3. Grid Generation

Hexahedral trimmed grids were generated by using the mesh tools in STAR-CCM+. Figure 4 shows the grid generation in the computational domain, including the grids of the background region and overset region. The size of the background region was the same as that of the computational domain. The size of the overset region was designed as $-0.2L < X < 1.2L$, $0.0L < Y < 1.0L$, and $-0.4L + COG_z < Z < 0.4L + COG_z$. The grids near the free surface were refined at two levels to obtain an accurate free surface and deal with its large deformation. The vertical range of the free surface refinement region was specified as $-0.25L < Z < 0.25L$. The grids near the seaplane model were also refined, and four layers of the prismatic layer mesh were generated to accurately simulate the flow in the turbulent boundary layers. The height of the prismatic layers in the body-fitted mesh was estimated according to the thickness of turbulent boundary layers over a flat plate. The height of the first layer grid near the wall surface was determined by $y^+ = 30$.

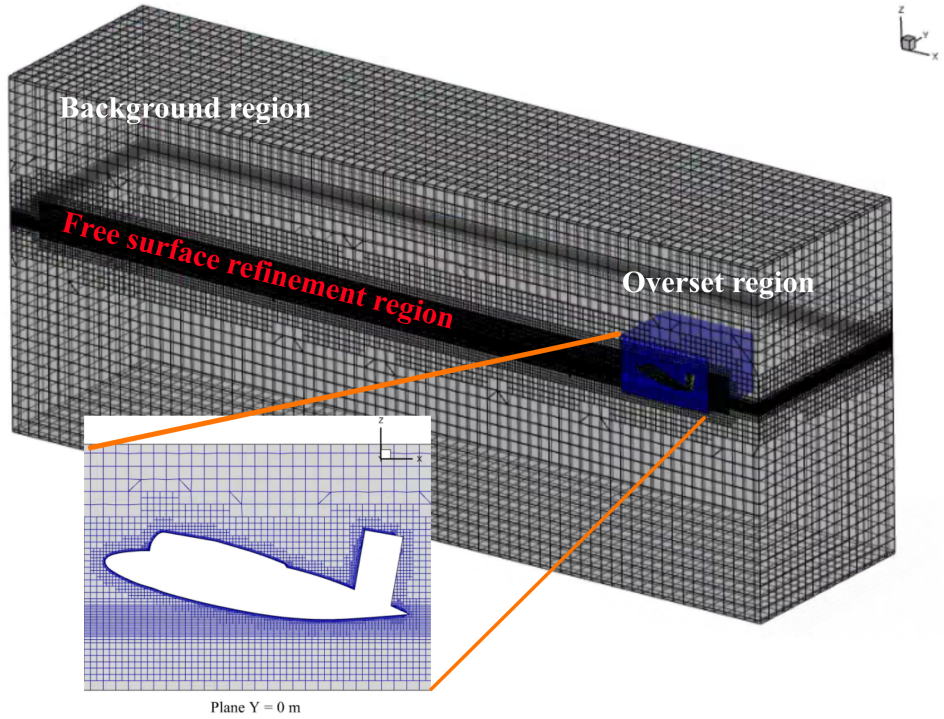


Figure 4. Grid generation of the background region, overset region, and grid refinements.

4. Numerical Results and Discussions

4.1. Verification and Validation

The convergence studies on the grid size and time step for the numerical simulations of ditching on calm water were firstly carried out for verification. The case set-ups for the convergence studies were based on the experimental condition [22]. For the condition of the seaplane model, the initial horizontal velocity was $U_0 = 50$ ft/s (15.240 m/s) and the initial pitch angle was $\theta_0 = 10°$. The initial vertical velocity of the plane was set as $V_0 = 0$ m/s. For the environmental conditions, the plane ditched on calm water with no wind and no water current. The density of the water was 997.561 kg/m^3, and that of the air was 1.184 kg/m^3, respectively. The dynamic viscosity of the water w 8.887×10^{-4} Pa·s. The numerical simulation started from the time when the lowest point of the fuselage touched the water surface. For body motions, three DoF motions including the surge, heave and pitch, were freed and the other three-degree-of-freedom motions were fixed.

Three sets of grids were generated for the spatial convergence study with different grid sizes, which are listed in Table 2. The grid size near the moving wall boundary, Δl, was decreased from 0.01 m for the Coarse grid set to 0.004 m for the Fine grid set. N_1,

N_2, and N_t stand for the number of grids in the background region, the overset region, and the total number of grids, respectively. With the refinement of the grids, N_t ranged from 169 million to 752 million. The time step was specified based on a CFL number of 0.7 for all cases. The time histories of the magnitude of the horizontal velocity, $|U|$, and the pitch angle, θ, of the plane model are shown in Figure 5a and Figure 5b, respectively. It can be indicated that the numerical solutions converged as the grid was refined from Coarse to Fine. Considering the balance of computational cost and accuracy, the medium grid set was used in the following studies.

Furthermore, the temporal convergence study was carried out by applying three cases with different time steps, i.e., TS1, TS2, and TS3, as presented in Table 3. Based on the mesh with the medium grid size, the time step and the corresponding CFL number were decreased from TS1 to TS3. Note that the CFL number should not be too large in case the numerical iterations diverge. Figure 6 shows the predicted $|U|$ and θ of the plane model for cases with different time steps. Converged time series of the velocity and pitch angle were obtained as the time step was decreased. Finally, a time step of $\Delta_t = 0.0015$ s was determined as the converged case, and the corresponding CFL number of 0.7 was adopted in the following studies.

Table 2. Cases of the convergence study on the grid size.

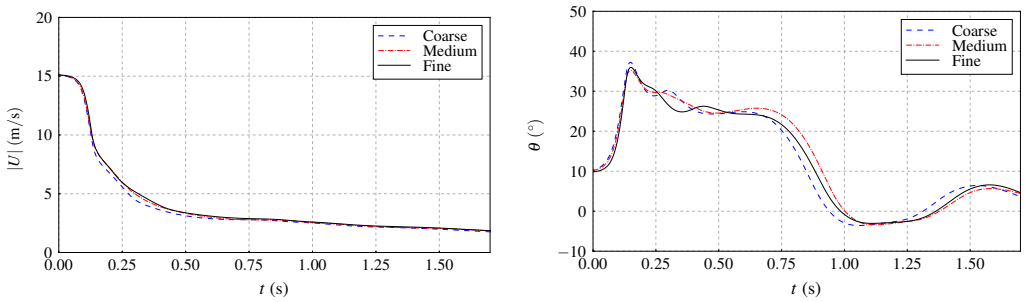
Grid Sets	Δl (m)	N_1	N_2	N_t
Coarse	0.010	1,567,057	124,738	1,691,795
Medium	0.007	4,331,304	298,393	4,629,697
Fine	0.004	6,417,224	1107,193	7,524,417

Table 3. Cases of the convergence study on the time step.

Time Steps	Δt (s)	CFL
TS1	0.0025	1.3
TS2	0.0020	1.0
TS3	0.0015	0.7

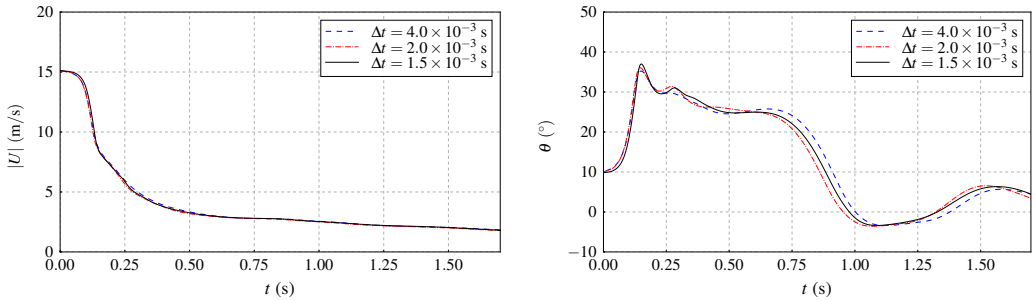
The numerical solutions obtained by using the best-practice settings, i.e., the medium grid set and a CFL number of 0.7, were compared with the experimental data [22] for validation. While the plane was ditching on calm water, the horizontal velocity decreased heavily in the stage of slamming ($0 < t < 0.2$ s). After slamming ($t > 0.2$ s), the plane then taxied in the water and the horizontal acceleration of the plane decreased. For the pitch angle, the peak value was obtained at about $t = 0.2$ s, which decreased twice and reached its lowest point ($t = 1.0$ s) during the plane taxiing in the water. After that, when $t > 1.0$ s, the pitch angle increased slowly to a small culmination and decreased finally. As shown in Figure 7, the predicted horizontal velocity and the maximum pitch angle were in good agreement with the experimental data. The change in pitch angle by the present simulation had a similar trend as that by the experimental measurement. The error between the numerical result and the experimental data could be caused by the limitations of the body motions and initial timing points. Three-degree-of-freedom body motions were only considered in the numerical simulations while the full coupled body motions of six degrees of freedom were freed in the experiments. In conclusion, the numerical results in the present work were verified and validated by convergence studies and by comparison to the experimental data. In this case, the volume fraction values of all grid cells were added up. Slamming occurred at about t = 0.2 s. The numerical results at a few times during/after the slamming are shown in Figure 8. It can be observed that the volume fraction value changed a little and the convergence of the simulation was proven. The hydrodynamic pressure on the midsection of the plane at the time t = 0.2 s during slamming is presented in Figure 9. The stagnation point can be seen at the location of the maximum pressure point,

i.e., $x = -0.35$ m. The jet flow near the fuselage during the water entry process is shown in Figure 10. At the time $t = 0.2$ s, slamming occurred at the rear bottom of the fuselage. The flow was attached to the body surface. At the time $t = 0.5$ s, separation of the jet flow can be observed. The water ran up from the fuselage and impacted the wings. After that, the jet flow dropped, which can be seen at the time $t = 0.8$ s. The slamming was not violent in the vertical direction under the condition that the initial vertical velocity of the plane was zero.



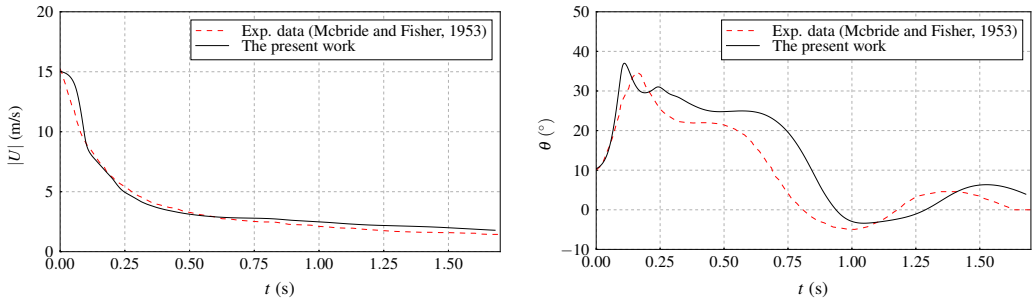
(**a**) (**b**)

Figure 5. Convergence of numerical results on grid sizes: (**a**) Horizontal velocity. (**b**) Pitch angle.



(**a**) (**b**)

Figure 6. Convergence of numerical results on time steps: (**a**) Horizontal velocity. (**b**) Pitch angle.



(**a**) (**b**)

Figure 7. Validation of numerical results in comparison with the experimental data [22]: (**a**) Horizontal velocity. (**b**) Pitch angle.

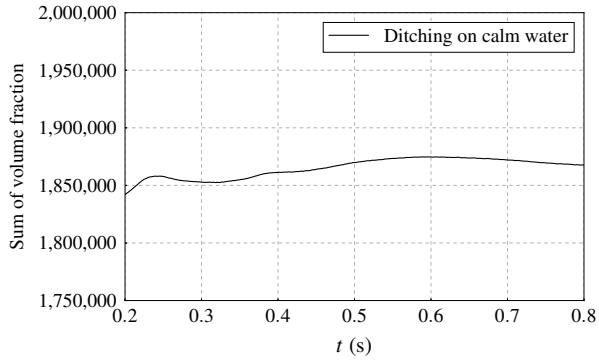


Figure 8. The sum of volume fraction in the flow field for ditching on calm water.

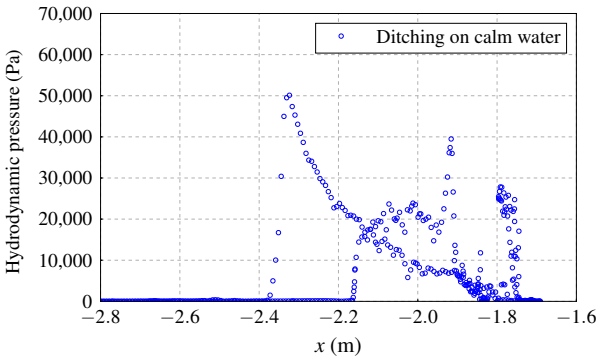


Figure 9. The hydrodynamic pressure at $t = 0.2$ s during slamming for ditching on calm water.

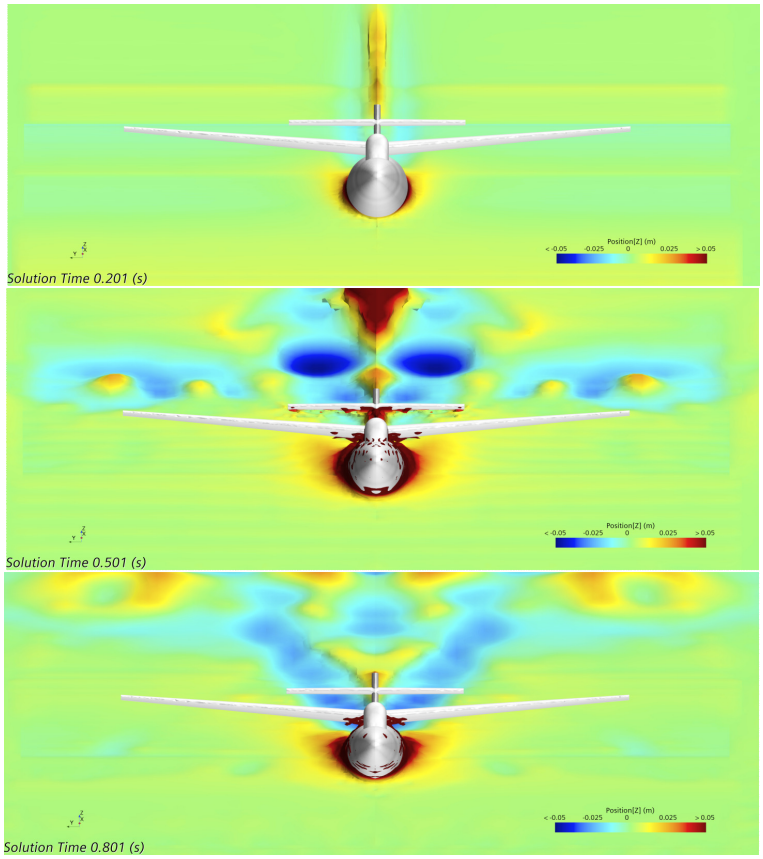


Figure 10. Separation of the jet flow during slamming for ditching on calm water.

4.2. Ditching on Calm Water

In this paper, the seaplane ditching on calm water with different initial velocities and initial trim angles was comprehensively investigated by using the best-practice settings. The ditching performance was analyzed including the motion responses of the coupled surge, heave, and pitch motions and hydrodynamic loads. Hydrodynamic loads are composed of the vertical and horizontal forces and the rotational moment along the y-axis. In addition, local pressures on three pressure probes on the body surface, i.e., P1, P2, and P3, were recorded to investigate the local slamming pressures during the plane model ditching on calm water. The sketch of the probe position is shown in Figure 11, and the initial coordinates of the pressure probes are presented in Table 4. It should be noted that the probe points are always fixed on the body surface, which means their coordinates are changing according to the motions of the plane model. The probes P1 and P3 were set on the bottom of the head and tail of the fuselage, respectively. The probe P2 was located at the middle point on the bottom of the fuselage.

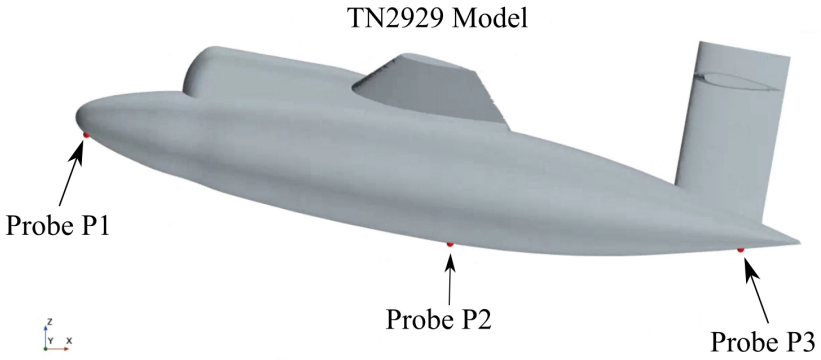


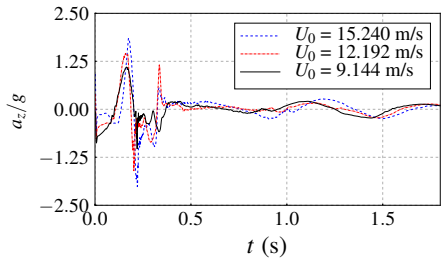
Figure 11. Sketch of the pressure probes on the body surface.

Table 4. Initial coordinates of the pressure probes on the body surface.

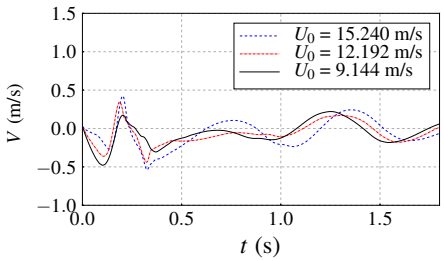
Probes	X (m)	Y (m)	Z (m)
P1	0.0361	0.0010	0.2033
P2	0.6345	0.0010	0.0239
P3	1.1128	0.0010	0.0147

Time histories of the motion responses of the TN2929 model ditching on calm water with various initial velocities are shown in Figure 12. The initial horizontal velocities were $U_0 = 15.240$ m/s, 12.192 m/s, and 9.144 m/s, while the initial vertical velocity was 0 m/s. Figure 12a,d present the translational accelerations along the z and x directions, respectively. The numerical results were non-dimensionalized by dividing the acceleration of gravity ($g = 9.81$ m/s^2). A negative value means the result of acceleration is toward the negative z or negative x direction. It can be seen that the vertical acceleration was increased from g to the first peak value, decreased heavily during the ditching process, and then, increased. After several oscillations, the vertical acceleration was increased to its second peak, which was followed by a decrease in vertical acceleration. The oscillations of the vertical acceleration were roughly suppressed and varied slowly around the position of equilibrium. With the increase of the initial horizontal velocity, the peak value of a_z or a_x became higher and the maximum vertical acceleration reached $1.8g$. The difference between the maximum and minimum vertical acceleration was $3.6g$. For the second peak value, the result of $U_0 = 15.240$ m/s was smaller than that of $U_0 = 12.192$ m/s, while that of $U_0 = 9.144$ m/s was the smallest. The horizontal accelerations in the three cases were all positive. Only one peak was found for the result of $U_0 = 9.144$ m/s. Two peaks including a large peak and a small one can be observed with $t < 0.5$ s. The maximum horizontal acceleration reached a value of $14.5g$. Figure 12b shows the vertical velocity decreasing

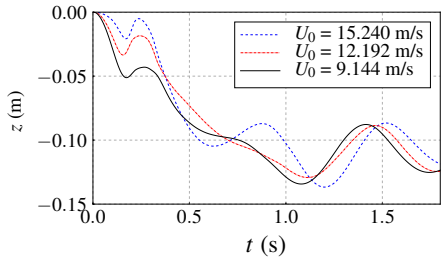
from zero due to gravity and increasing under the fluid force. Several oscillations happened after slamming while the plane was ditching on calm water. The vertical displacement is shown in Figure 12c. The plane was plunging into the water with an increasing negative value of the z coordinate. After slamming with $t > 0.5$ s, the oscillated vertical displacement can be seen and the equilibrium can be obtained near $z = -0.12$ m. Figure 12e,f show the horizontal velocity and displacement. Similar trends in the numerical results of various U_0 were observed. In particular, the horizontal velocities decreased, and the final stable velocity was independent of U_0. The rotational acceleration of the plane was first increased, then decreased heavily to a minimum value and increased briefly to zero, as shown in Figure 12g. The higher absolute value of α was found with a larger U_0. The change in rotational acceleration was similar to a pulse function in a negative direction at the time of slamming. The angular velocity and pitch angle are presented in Figure 12h,i, respectively. A large peak of the angular velocity can be found, which was proportional to the value of U_0. A maximum pitch angle of 37° was found during the slamming. The initial horizontal velocity had an important influence on the secondary oscillations of θ. Despite the phase, the peak pitch angle did not vary much for the cases with different U_0.



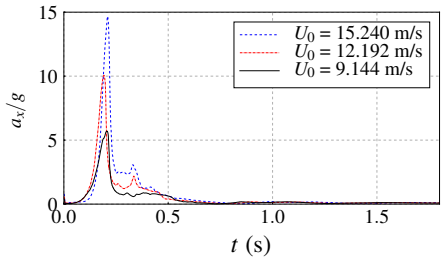
(**a**) Vertical acceleration



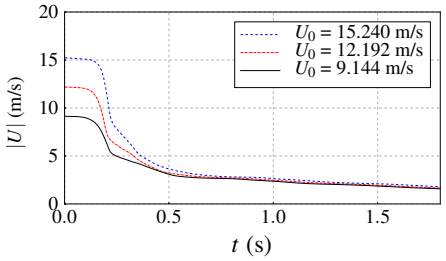
(**b**) Vertical velocity



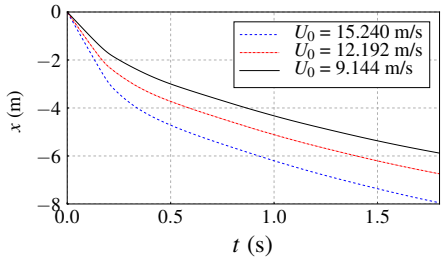
(**c**) Vertical displacement



(**d**) Horizontal acceleration

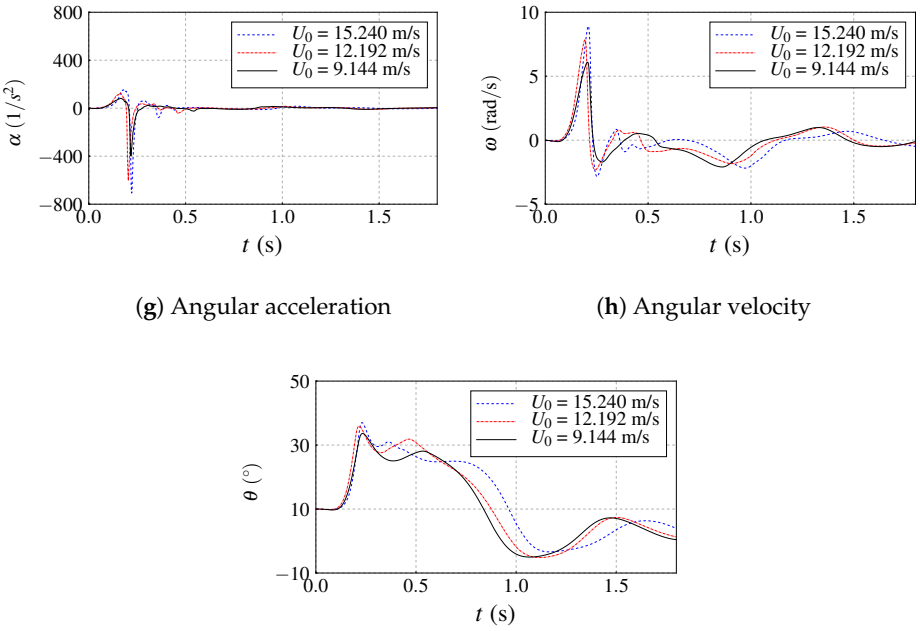


(**e**) Horizontal velocity



(**f**) Horizontal displacement

Figure 12. *Cont.*



(**g**) Angular acceleration (**h**) Angular velocity

(**i**) Pitch angle

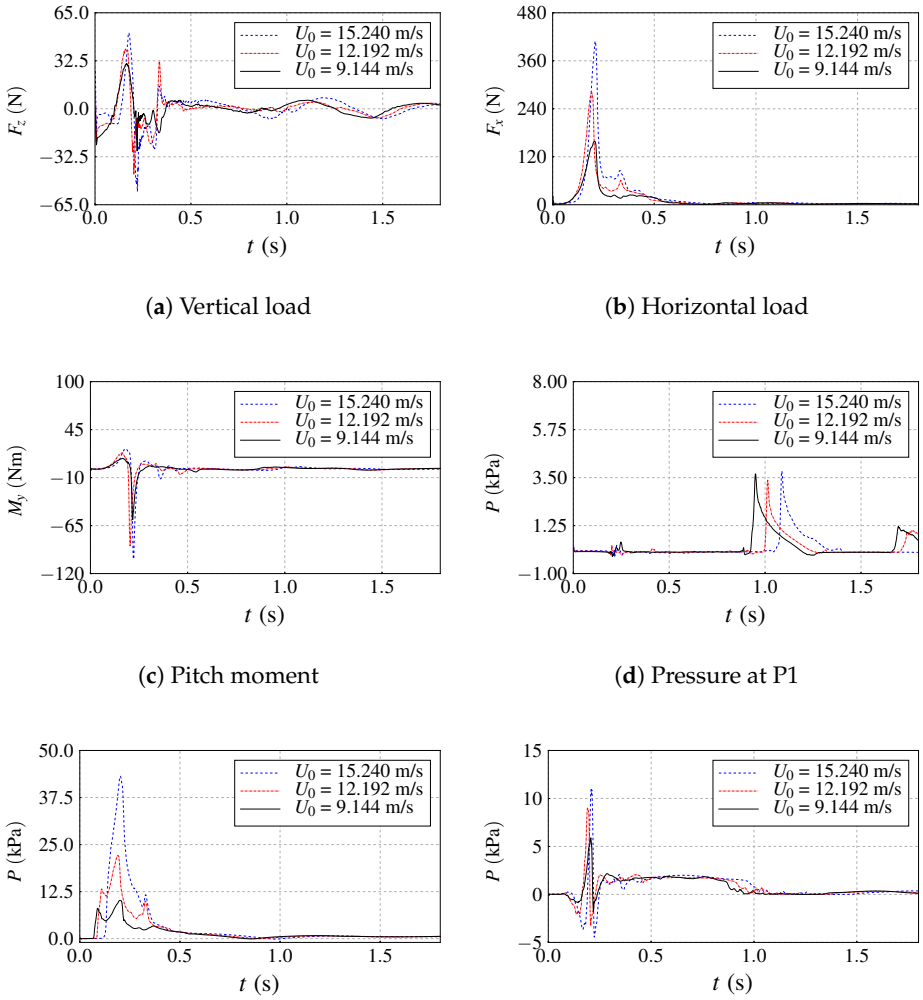
Figure 12. Time domain motion responses of TN2929 model ditching on calm water with various initial velocities.

Figure 13 shows how the total loads and local pressures changed over time as the TN2929 model ditched on calm water at different starting speeds. The predicted vertical loads, horizontal loads, and pitch moment of the plane with three U_0 are shown in Figure 13a–c, which are similar to the results of the vertical, horizontal, and angular accelerations. Regarding the local pressures at P1, P2, and P3, which are presented in Figure 13d–f, the slamming pressures were greatly affected by the initial horizontal velocity. Note that the initial pitch angle was set as 10°, and the probe P1 was not immersed in the water at the beginning of slamming. The peak pressures at P2 and P3 were obtained earlier than those at P1, while two peak pressures at P1 were observed during the plane ditching on calm water. In addition, the maximum pressure at P2 was higher than that at P1 and P3 during the slamming. The peak pressure reached as high as 45 kPa for the case with an initial horizontal velocity of $U_0 = 15.240$ m/s for the TN2929 model ditching on calm water. A smaller U_0 led to a lower impulse pressure and an earlier impact time for pressures at all the probes. It can be indicated that the difference between the peak pressure at P1 was not substantial with the three present values of U_0.

The time evolutions of the motion responses of the plane ditching on calm water with various initial pitch angles are shown in Figure 14. For example, the vertical acceleration of the plane for $\theta_0 = 20°$ reached $4g$, which became the highest acceleration among the results for those three θ_0. In terms of the result for $\theta_0 = 30°$, a_z was decreased to $-2.8g$ and, then, increased, as shown in Figure 14a. The reason should be that the vertical fluid force was smaller than the gravitational force when $t < 0.2$ s. Figure 14b,c show similar trends of the vertical velocity and displacement with oscillations. The value of θ_0 had a great impact on the peak vertical velocity and displacement. With the increasing θ_0, larger-amplitude vertical motions of the plane can be generated during the ditching. The horizontal accelerations of the plane with θ_0 are shown in Figure 14d. The peak horizontal acceleration occurred later for $\theta_0 = 20°$, while the time at the peak a_x/g was close for $\theta_0 = 10°$ and $\theta_0 = 30°$. The maximum horizontal acceleration was decreased for $\theta_0 = 30°$. As shown in Figure 14e,f, the evolutions of the horizontal velocity and displacement changed similarly for $\theta_0 = 10°$ and $\theta_0 = 30°$. For $\theta_0 = 20°$, a delay can

be observed. The final results of the horizontal velocities for various θ_0 were basically the same. The rotational motions of the plane ditching on calm water were also affected by changing the values of θ_0, as presented in Figure 14g–i. The impulses of the angular acceleration and velocity occurred for $\theta_0 = 10^\circ$ and $\theta_0 = 20^\circ$, while a smaller angular acceleration or velocity was obtained for $\theta_0 = 30^\circ$ with oscillations. The pitch angles for $\theta_0 = 10^\circ$ and $\theta_0 = 30^\circ$ both increased firstly and, then, decreased. However, θ decreased when $t < 0.4$ s and, then, increased to the maximum value for $\theta_0 = 20^\circ$. This feature could be caused by the differences in aerodynamic lift forces for various θ_0.

The total loads and local pressures of the model ditching with various initial pitch angles are shown in Figure 15. The numerical results of the vertical loads, horizontal loads, and pitch moment with three θ_0 were similar to the results of the vertical, horizontal, and angular accelerations, as presented in Figure 13a–c. The initial pitch angle also had an impact on the local pressures. Figure 13d shows that, at the time $t = 1.0$ s for $\theta_0 = 30^\circ$, the water was overtopping on the head of the fuselage, which led to fluctuations in the slamming pressures after the peak values of the pressure at P1 were reached. It is indicated in Figure 13e,f that, for $\theta_0 = 20^\circ$, the peak pressure at P2 was the lowest, while that at P3 was the highest. The fluctuations of the pressure at P3 can be found for $\theta_0 = 30^\circ$.



(**a**) Vertical load

(**b**) Horizontal load

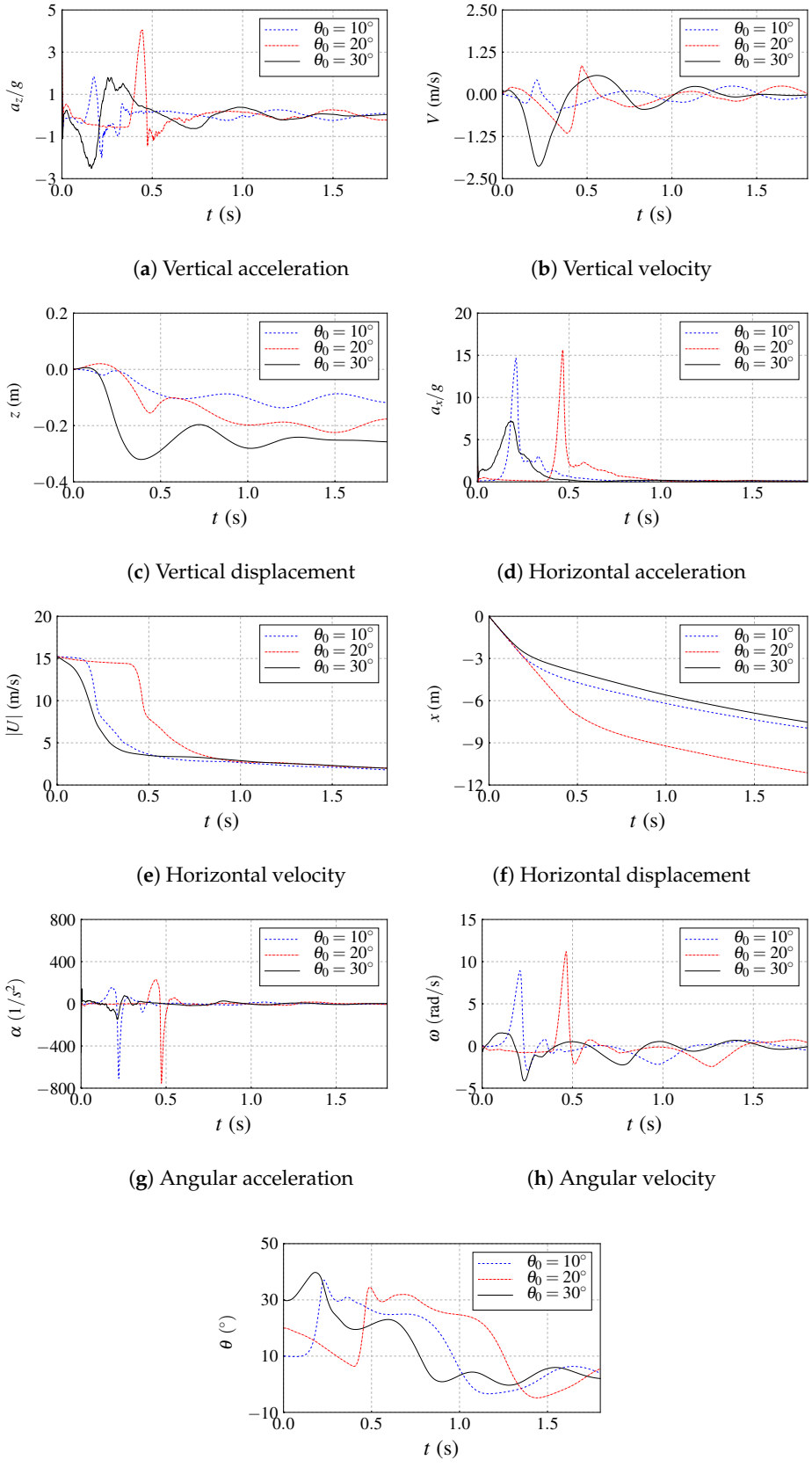
(**c**) Pitch moment

(**d**) Pressure at P1

(**e**) Pressure at P2

(**f**) Pressure at P3

Figure 13. Total loads and local pressures of TN2929 model ditching on calm water with various velocities.



(**a**) Vertical acceleration (**b**) Vertical velocity

(**c**) Vertical displacement (**d**) Horizontal acceleration

(**e**) Horizontal velocity (**f**) Horizontal displacement

(**g**) Angular acceleration (**h**) Angular velocity

(**i**) Pitch angle

Figure 14. Time domain motion responses of TN2929 model ditching on calm water with different initial angles.

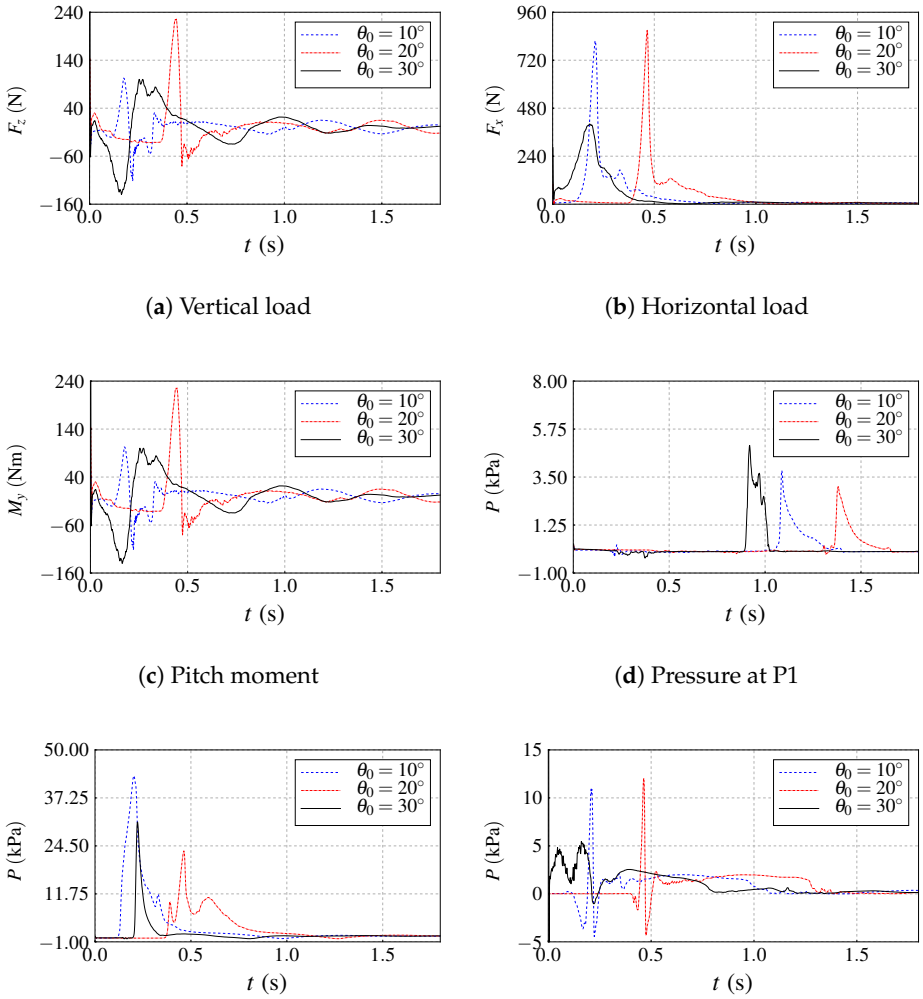


Figure 15. Total loads and local pressures of TN2929 model ditching on calm water with different initial angles.

The change of the free surface at different instants of time during the ditching of the TN2929 model is captured in Figure 16. The initial settings of the horizontal velocity and the pitch angle were $U_0 = 15.240$ m/s and $\theta_0 = 10°$. Two stages of the ditching can be analyzed including the stage of slamming ($0 < t < 1.5$ s) and the stage of taxiing ($t > 1.5$ s). For the stage of slamming, the bottom of the fuselage tail first entered the water at $t = 0.15$ s due to the initial inclined angle. The wave near the tail was generated and flowed over the fuselage surface at $t = 0.18$ s. With the increase of the pitch angle of the plane, waves were developed at $0.18 < t < 0.75$ s. A main crest and two troughs in the wake field can be observed at $t = 0.45$ s. Splashing water and the large deformation of the free surface during the slamming were caused by the plane motions, for example at $t = 0.45$ s and $t = 0.75$ s. The bottom of the fuselage head then entered the water at $t = 1.20$ s. In particular, the model was overwashed with water flow overtopping the fuselage head and tail. After $t = 1.50$ s, the body motions of the plane were suppressed at the stage of taxiing. The wave wake was similar to a ship advancing in calm water with a Kelvin wave system. Bow waves can be found near the fuselage head at $t = 1.8$ s.

Figure 17 shows the comparisons of the free surfaces and pressure contours during the ditching of the TN2929 model with various initial horizontal velocities. As an example, at $t = 0.45$ s, all cases for $\theta_0 = 10°$ were characterized by a main wave crest and two

wave troughs in the wake field. The larger U_0 can cause higher waves during the ditching because of the higher kinetic energies. There were several low points of the free surface of the plane with a $U_0 = 12.192$ m/s. This could be caused by the wing vortex. The pressure contours show similar distributions of the hydrodynamic pressure on the bottom surface of the fuselage. A high-pressure region was mainly located at the front central triangular area. The comparisons of the free surfaces and pressure contours with different initial pitch angles are presented in Figure 18. The initial horizontal velocity of the plane was set as $U_0 = 15.240$ m/s. At $t = 0.45$ s, the plane with $\theta_0 = 20^\circ$ was still at an early stage of slamming, and the free surface was smoother than the cases for $\theta_0 = 10^\circ$ and $\theta_0 = 30^\circ$. The impact pressures on the fuselage bottom were higher than the results of the other two cases. The high pressures were distributed on the two ends of the fuselage for $\theta_0 = 30^\circ$.

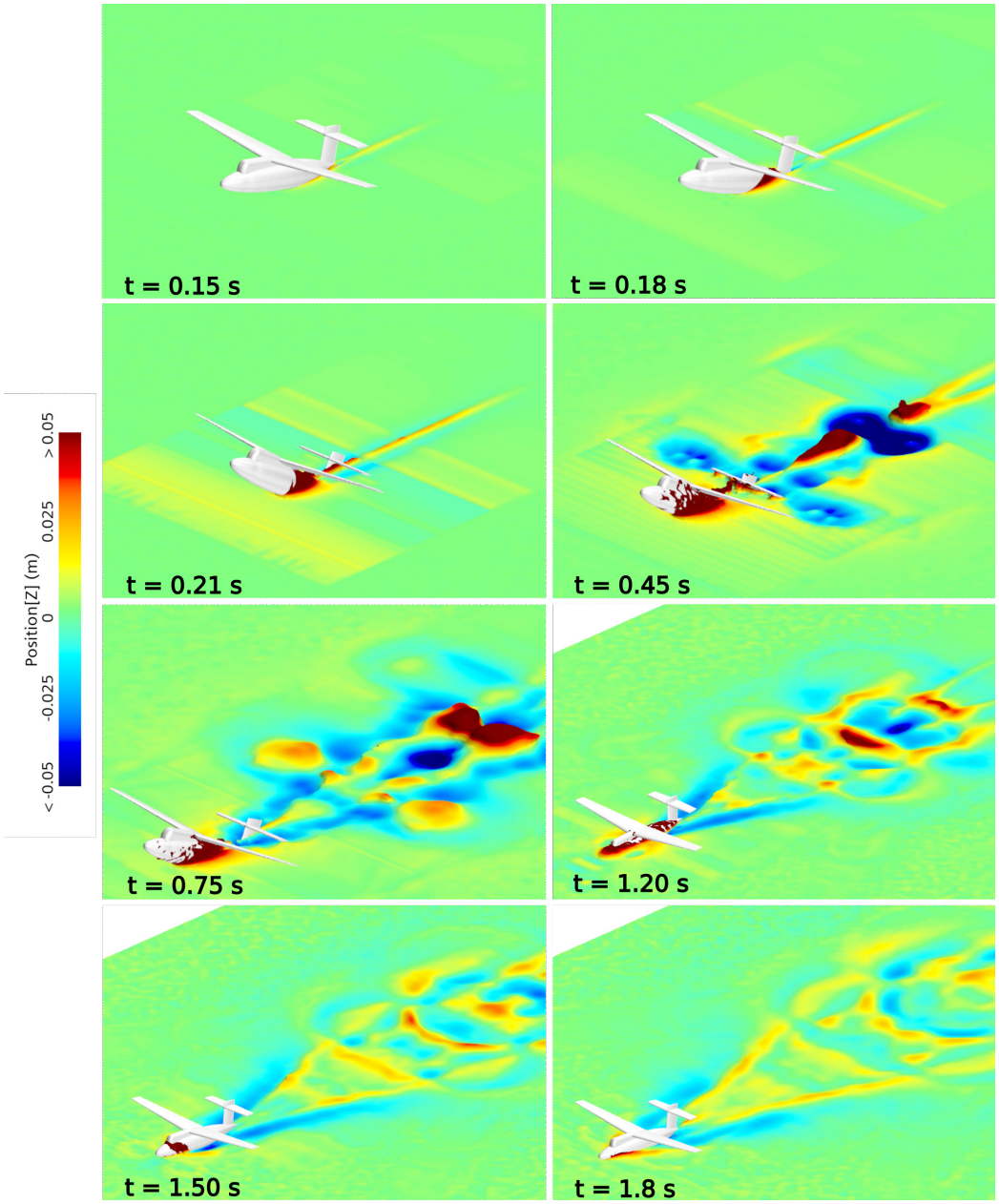


Figure 16. Snapshots of free surfaces during the ditching of the TN2929 model ($U_0 = 15.240$ m/s, $\theta_0 = 10^\circ$).

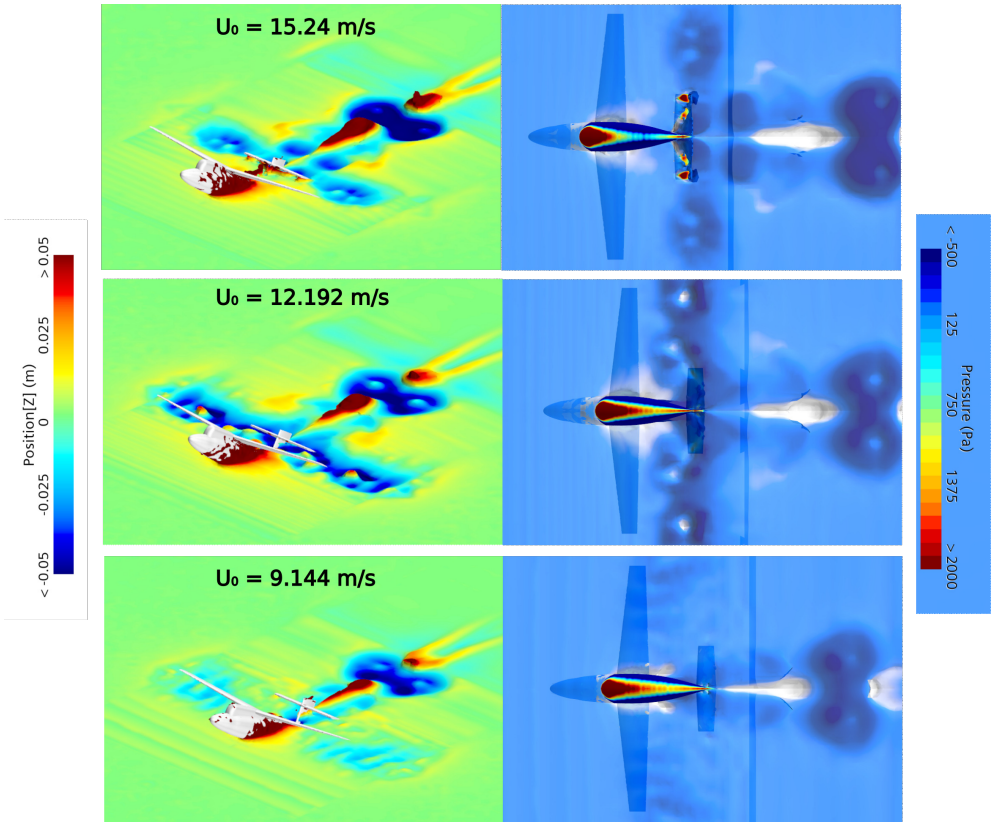


Figure 17. Comparisons of free surfaces and pressure contours during the ditching of TN2929 model with various initial horizontal velocities ($\theta_0 = 10°$).

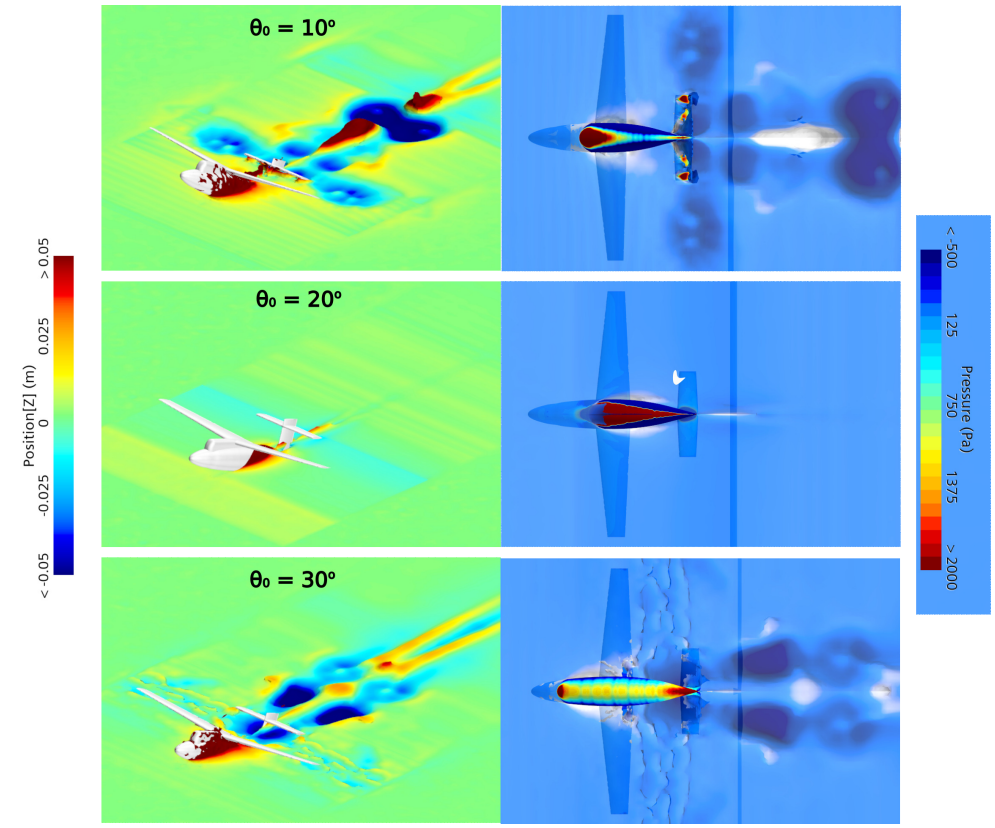


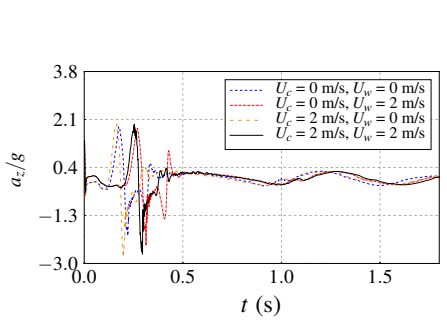
Figure 18. Comparisons of free surfaces and pressure contours during the ditching of TN2929 model with different initial pitch angles ($U_0 = 15.240$ m/s).

4.3. Ditching on Water with Current/Wind

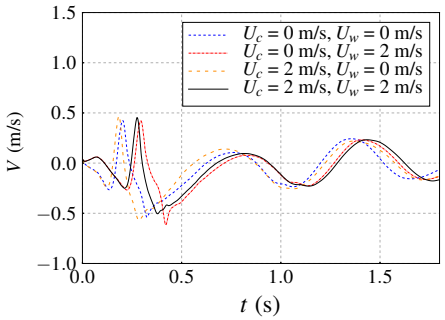
The effects of water current and wind on the motions and loads of the TN2929 model ditching on water are numerically investigated in this section. U_c and U_w denote the velocity of inflow current and wind velocity, respectively. The uniform inflow speed was chosen as 2 m/s. The results of the four cases were analyzed, including the calm water with no current/wind ($U_c = 0$ m/s, $U_w = 0$ m/s), the condition with the wind only ($U_c = 0$ m/s, $U_w = 2$ m/s), the condition with the current only ($U_c = 2$ m/s, $U_w = 0$ m/s), and the condition with the water current coupled with wind ($U_c = 2$ m/s, $U_w = 2$ m/s). For all cases of the TN2929 model ditching on the water with the current/wind, the initial horizontal velocity and the pitch angle were $U_0 = 15.240$ m/s and $\theta_0 = 10°$.

The time histories of the motion responses of the plane ditching on calm water with the uniform current and wind are shown in Figure 19a–i. The vertical acceleration, horizontal acceleration, and angular acceleration of the pitch motion in Figure 19a,d,g for the case with the current only were similar to those for the case with no current/wind (calm water). On the contrary, the results of the accelerations for the case with wind only were close to those for the case with the current coupled with the wind. It can be indicated that the wind had a greater effect on the accelerations of both the translational and rotational motions. The same conclusions can be drawn for the vertical velocity and angular velocity, as shown in Figure 19b,h. Figure 19e shows that the horizontal velocity was more related to the current instead of the wind. The phase of vertical displacement differed for the cases, and the effect of wind caused a delayed change of z, as shown in Figure 19c. Both the current and wind have impacts on the change of the horizontal displacement (Figure 19f). The phenomenon can be explained by the fact that the water current could increase the resistance force and the wind could increase the lift force. For the pitch angle, as shown in Figure 19i, the maximum pitch angles of the plane for all cases were close. The effect of the wind can slow the increase of the pitch angle at the stage of slamming.

Similarly, Figure 20a–c show that the results of the vertical loads, horizontal loads, and pitch moment with different conditions of the wind and the current were similar to the results of the vertical, horizontal, and angular accelerations. The local pressures in the time domain at P1, P2, and P3 of the plane are compared in Figure 20d–f. The peak pressure at the fuselage head (P1) or tail (P3) of slamming was close for all cases, while the time up to the peak was delayed for the cases with wind. In addition, the peak pressure at the center of the fuselage (P2) was increased by the effect of the water current since the relative velocity between the plane and the water was increased. The wind had little influence on the peak pressure of slamming in comparison to the cases with the current.

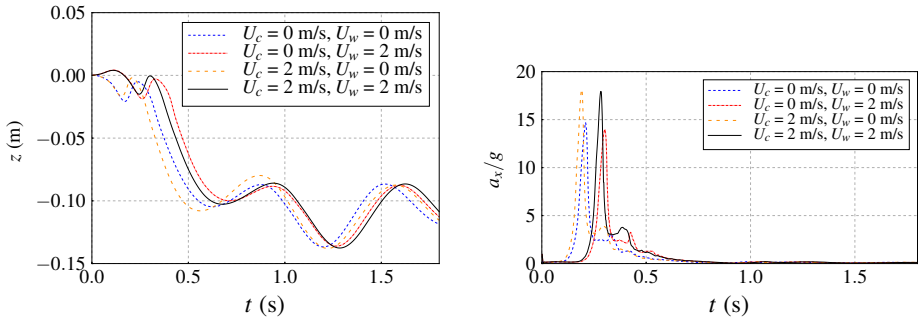


(**a**) Vertical acceleration



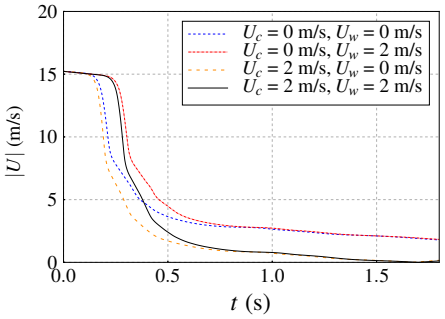
(**b**) Vertical velocity

Figure 19. *Cont.*

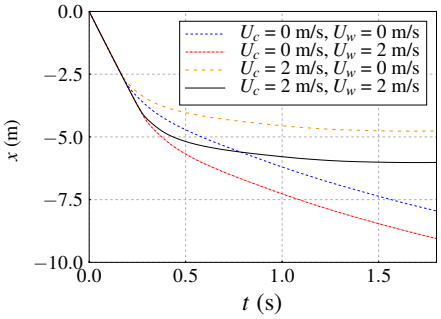


(**c**) Vertical displacement

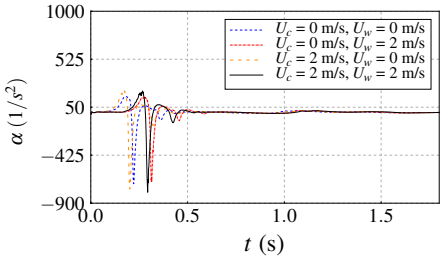
(**d**) Horizontal acceleration



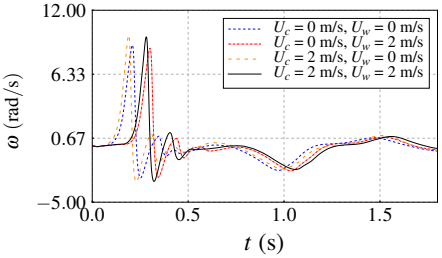
(**e**) Horizontal velocity



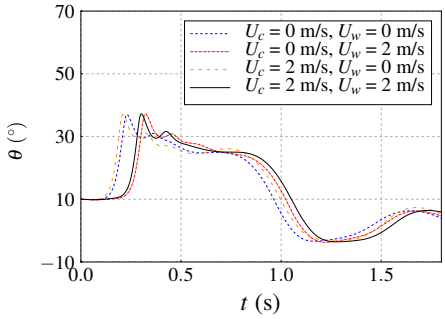
(**f**) Horizontal displacement



(**g**) Angular acceleration

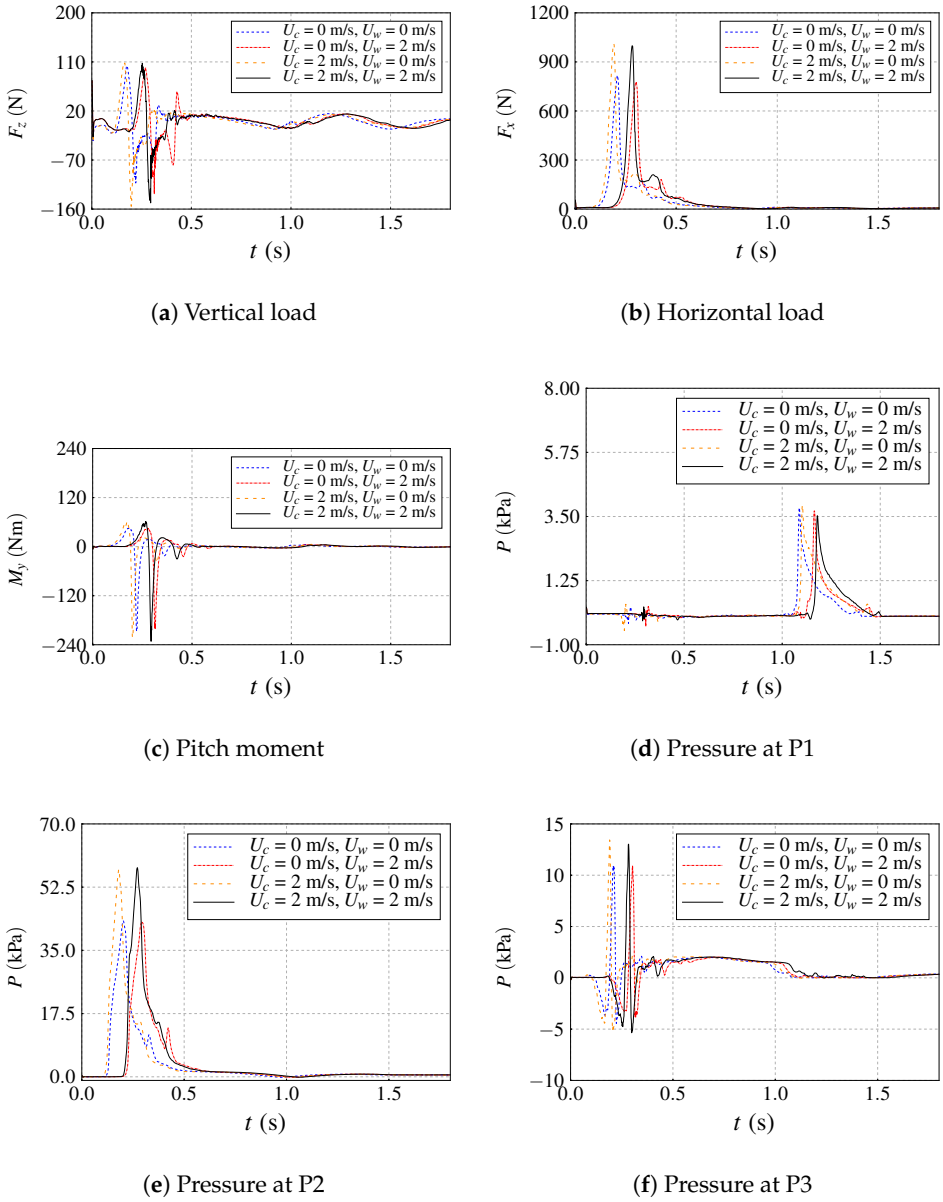


(**h**) Angular velocity



(**i**) Pitch angle

Figure 19. Time domain motion responses of TN2929 model ditching on water with uniform current and wind.



(**a**) Vertical load

(**b**) Horizontal load

(**c**) Pitch moment

(**d**) Pressure at P1

(**e**) Pressure at P2

(**f**) Pressure at P3

Figure 20. Total loads and local pressures of TN2929 model ditching on water with current and wind.

The evolutions of the water–air free surface and pressure contours of the cases with the water current and wind are compared in Figure 21. The numerical results of the case with current only were generally the same as those of the case with no current and no wind. The wave troughs behind the fuselage became deeper under the condition of water current. The free surface and the pressure contour of the case with wind only were similar to those of the case with water current coupled with wind. The water elevations under the plane wing were lower for the case with wind only than those of other cases.

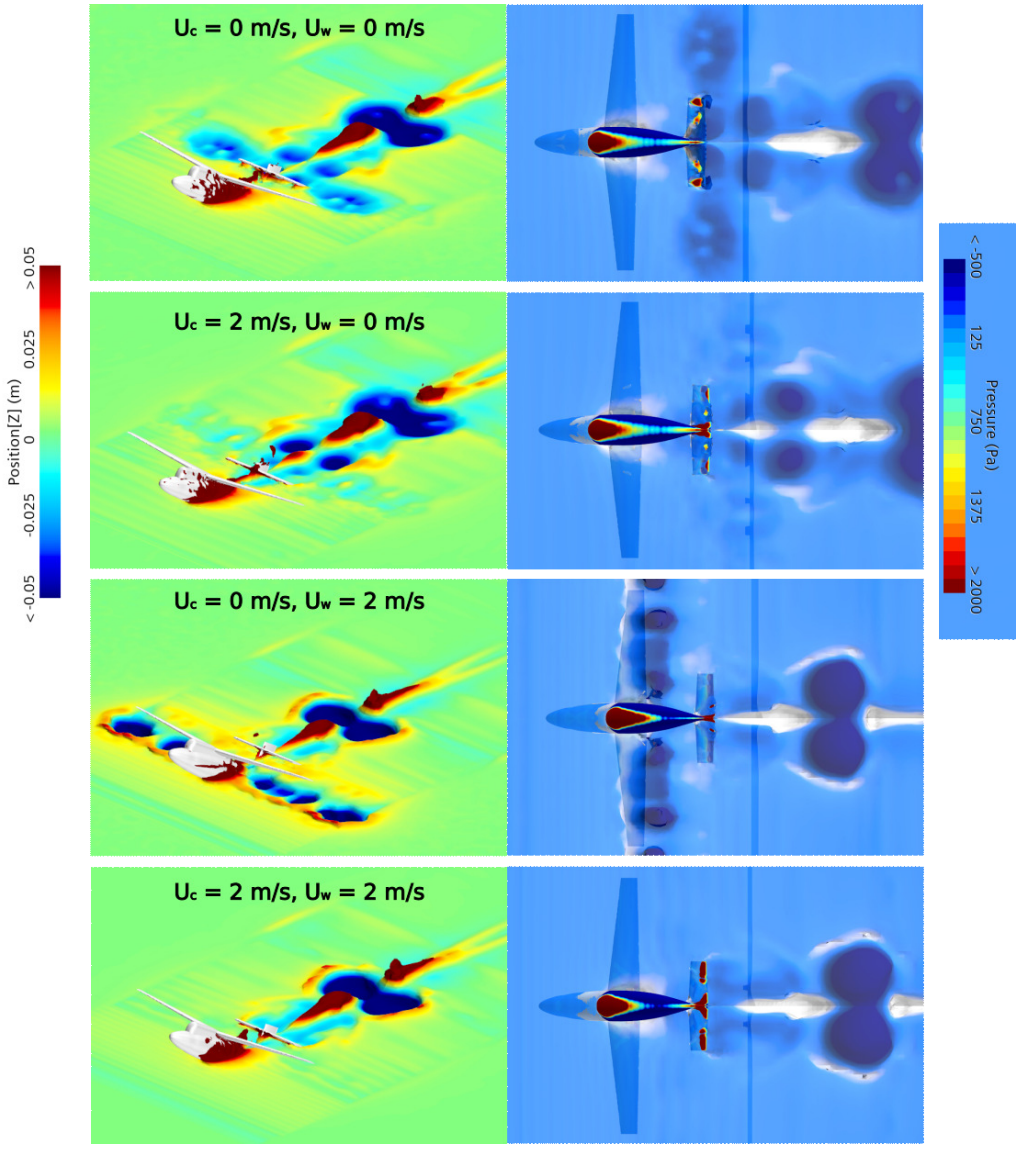


Figure 21. Comparisons of free surfaces and pressure contours during the ditching of TN2929 model with current and wind ($U_0 = 15.240$ m/s, $\theta_0 = 10°$).

5. Conclusions

The ditching performance including the motion responses and loads of a seaplane model, i.e., the NACA TN2929 model A, was numerically studied by using the CFD software STAR-CCM+ 17.04.008-R8. The condition that could lead to the most-dangerous landing on water with the highest hydrodynamic loads and the largest motion responses was found. In addition, the wind had less effect than the water current on the amplitude of the slamming loads and motions. The spatial and temporal convergence studies indicated that the numerical results converged and a medium refinement of the grid set with a CFL of 0.7 was the best-practice settings. The results of the plane ditching on calm water with an initial horizontal velocity $U_0 = 15.240$ m/s and an initial pitch angle $\theta_0 = 10°$ were in good agreement with the experimental data, and the numerical methods were then validated. The overset grid technique and the VOF method were able to simulate the large-amplitude body motions with coupled translations and rotations and the large deformation of the free surface when the plane was ditching on the water. The ditching characteristics of the plane model were deeply related to the various initial horizontal velocities, initial pitch angle, and the condition of the water current/wind. During the stage of slamming, the fuselage head, the middle body, and the rear fuselage could experience huge impulse

slamming pressures within a local region. The overwash of the water on the head and tail was observed due to the relative large motions between the water and the plane model. Based on the present numerical results, the conclusions are detailed as follows:

- The motion amplitude and accelerations can be increased by increasing the initial horizontal velocity of the plane, U_0. A higher U_0 means more kinetic energy can be transferred to the fluid energies, and therefore, the plane velocity must be controlled before the plane ditches on calm water. The peak of the local pressure at the probe P1 was little affected by changing U_0. However, the impact time at P1 was delayed for a higher U_0. For the local pressure at P2 and P3, the impact time was almost the same for the cases with various U_0.
- The motion responses of the case with the initial pitch angle $\theta_0 = 20^\circ$ were the largest in comparison with the results of the cases with $\theta_0 = 10^\circ$ and $\theta_0 = 30^\circ$. The first impact time of the local pressures at probes P1, P2, and P3 was also longer for the case with $\theta_0 > 10^\circ$. Therefore, the initial pitch angle should not be close to $\theta_0 = 20^\circ$.
- The effects of wind and current on the ditching performance of the TN2929 model were explained. The water current in the opposite direction of the advancing plane led to an increase in the horizontal loads, while the vertical loads were less affected by the current. The wind in the opposite direction of the advancing plane had little influence on the amplitude of slamming loads and motions. However, the wind was able to delay the impact time for the total loads and local pressures.

Author Contributions: Conceptualization, R.Z. and K.W.; methodology, R.Z. and J.S.; software, H.T. and Q.H.; validation, R.Z., K.W. and J.S.; formal analysis, H.T.; investigation, R.Z.; resources, R.Z. and J.S.; data curation, R.Z.; writing—original draft preparation, R.Z.; writing—review and editing, R.Z. and K.W.; visualization, R.Z.; supervision, R.Z.; project administration, R.Z.; funding acquisition, R.Z. and K.W. All authors have read and agreed to the published version of the manuscript.

Funding: This research was funded by the National Natural Science Foundation of China (52201394, 52171289), the National Key Research and Development Program of China (No. 2022YFC2806300), the Innovation Group Project of Southern Marine Science and Engineering Guangdong Laboratory (Zhuhai) (No. 311023014), and the Special Fund for promoting high-quality economic development of province in 2022 from Department of Natural Resources of Guangdong Province (Grant No. GDNRC[2022]023, GDNRC[2022]028).

Institutional Review Board Statement: Not applicable.

Informed Consent Statement: Not applicable.

Data Availability Statement: The raw data supporting the conclusions of this article will be made available by the authors upon request.

Conflicts of Interest: The authors declare no conflicts of interest.

References

1. Kanyoo, P. Mathematical Model of High Speed Planing Dynamics and Application to Aircraft Ditching. Ph.D. Thesis, University of Southampton, Southampton, UK, **2016**.
2. Lou, B.; Wang, G.; Huang, Z.; Ye, S. Preliminary design and performance analysis of a solar-powered unmanned seaplane. *Proc. Inst. Mech. Eng. Part G J. Aerosp. Eng.* **2019**, *233*, 5606–5617. [CrossRef]
3. Karman, T.V. The impact of seaplane floats during landing. In *National Advisory Committee for Aeronautics Technical Report Archive & Image Library*; NASA: Washington, DC, USA, 1929.
4. Wagner, H. Über stoß-und gleitvorgänge an der oberfläche von flüssigkeiten. *ZAMM-J. Appl. Math. Mech. Angew. Math. Mech.* **1932**, *12*, 193–215. [CrossRef]
5. Oliver, J. Second-order Wagner theory for two-dimensional water-entry problems at small deadrise angles. *J. Fluid Mech.* **2007**, *572*, 59–85. [CrossRef]
6. Chatjigeorgiou, I.K. An analytical approach for the three-dimensional water entry problem of solids creating elliptical contact regions. *J. Fluids Struct.* **2019**, *91*, 102703. [CrossRef]
7. Zhao, R.; Faltinsen, O.; Aarsnes, J. Water entry of arbitrary two-dimensional sections with and without flow separation. In Proceedings of the 21st Symposium on Naval Hydrodynamics, Trondheim, Norway, 24–28 June 1996; pp. 408–423.

8. Barjasteh, M.; Zeraatgar, H.; Javaherian, M.J. An experimental study on water entry of asymmetric wedges. *Appl. Ocean Res.* **2016**, *58*, 292–304. [CrossRef]
9. Zhang, Y.; Xu, F.; Cai, W.; Li, J. Experimental study on the impact response of different structures water entry. In Proceedings of the 2017 8th International Conference on Mechanical and Aerospace Engineering (ICMAE), Prague, Czech Republic, 22–25 July 2017; pp. 644–647.
10. Iafrati, A.; Grizzi, S. Cavitation and ventilation modalities during ditching. *Phys. Fluids* **2019**, *31*, 052101. [CrossRef]
11. Nicolosi, G.; Valpiani, F.; Grilli, G.; Saponaro Piacente, A.; Di Ianni, L.; Cestino, E.; Sapienza, V.; Polla, A.; Piana, P. Design of A Vertical Ditching Test. In Proceedings of the 32nd ICAS Congress, Shanghai, China, 6–10 September 2021; pp. 6–10.
12. Schellin, T.E.; Moctar, O.E. Numerical prediction of impact-related wave loads on ships. *J. Offshore Mech. Arct. Eng.* **2007**, *129*, 39–47. [CrossRef]
13. Qu, Q.; Hu, M.; Guo, H.; Liu, P.; Agarwal, R.K. Study of ditching characteristics of transport aircraft by global moving mesh method. *J. Aircr.* **2015**, *52*, 1550–1558. [CrossRef]
14. Qu, Q.; Liu, C.; Liu, P.; Guo, B.; Agarwal, R.K. Numerical simulation of water-landing performance of a regional aircraft. *J. Aircr.* **2016**, *53*, 1680–1689. [CrossRef]
15. Qi, H.; Bin, W.; Ming-Zhen, W.; Miao, H.; Rong, J. Numerical simulation of wave landing loads characteristics of twin-float seaplane. In Proceedings of the IOP Conference Series: Materials Science and Engineering, Kazimierz Dolny, Poland, 21–23 November 2019; Volume 692, p. 012024.
16. Zheng, Y.; Liu, P.; Qu, Q.; Wen, X.; Dai, J. Numerical Analysis of Porpoising Stability Limit of a Blended-Wing—Body Aircraft During Ditching. *J. Aircr.* **2023**, *60*, 348–354. [CrossRef]
17. Benmoussa, A.; Gamboa, P.V. Effect of Control Parameters on Hybrid Electric Propulsion UAV Performance for Various Flight Conditions: Parametric Study. *Appl. Mech.* **2023**, *4*, 493–513. [CrossRef]
18. Song, Z.; Deng, R.; Wu, T.; Duan, X.; Ren, H. Numerical simulation of planing motion and hydrodynamic performance of a seaplane in calm water and waves. *Eng. Appl. Comput. Fluid Mech.* **2023**, *17*, 2244028. [CrossRef]
19. Xiao, T.; Qin, N.; Lu, Z.; Sun, X.; Tong, M.; Wang, Z. Development of a smoothed particle hydrodynamics method and its application to aircraft ditching simulations. *Aerosp. Sci. Technol.* **2017**, *66*, 28–43. [CrossRef]
20. Woodgate, M.A.; Barakos, G.N.; Scrase, N.; Neville, T. Simulation of helicopter ditching using smoothed particle hydrodynamics. *Aerosp. Sci. Technol.* **2019**, *85*, 277–292. [CrossRef]
21. Xu, Y.; Sun, P.N.; Huang, X.T.; Marrone, S.; Geng, L.M. Numerical study of the splashing wave induced by a seaplane using mesh-based and particle-based methods. *Theor. Appl. Mech. Lett.* **2023**, *13*, 100463. [CrossRef]
22. Mcbride, E.E.; Fisher, L.J. Experimental investigation of the effect of rear-fuselage shape on ditching behavior. In *National Advisory Committee for Aeronautics Technical Report Archive & Image Library*; NASA: Washington, DC, USA, 1953.
23. Lai, Y.; So, R.; Anwer, M.; Hwang, B. Calculations of a curved-pipe flow using Reynolds stress closure. *Proc. Inst. Mech. Eng. Part C: Mech. Eng. Sci.* **1991**, *205*, 231–244. [CrossRef]
24. Spalart, P.; Allmaras, S. A one-equation turbulence model for aerodynamic flows. In Proceedings of the 30th Aerospace Sciences Meeting and Exhibit, Reno, NV, USA, 6–9 January 1992; p. 439.
25. Wilcox, D.C. Formulation of the kw turbulence model revisited. *AIAA J.* **2008**, *46*, 2823–2838. [CrossRef]
26. Menter, F.R. Two-equation eddy-viscosity turbulence models for engineering applications. *AIAA J.* **1994**, *32*, 1598–1605. [CrossRef]
27. Shih, T.H.; Liou, W.W.; Shabbir, A.; Yang, Z.; Zhu, J. A new $k-\epsilon$ eddy viscosity model for high Reynolds number turbulent flows. *Comput. Fluids* **1995**, *24*, 227–238. [CrossRef]
28. Mockett, C.; Fuchs, M.; Thiele, F. Progress in DES for wall-modelled LES of complex internal flows. *Comput. Fluids* **2012**, *65*, 44–55. [CrossRef]
29. Moukalled, F.; Mangani, L.; Darwish, M. The finite volume method. In *The Finite Volume Method in Computational Fluid Dynamics*; Springer: Berlin/Heidelberg, Germany, 2016; pp. 103–135.
30. Hu, Q.; Wang, M.Z.; Wu, B.; Zhang, J.X.; Xiao, Z. The Application of Overset Grid in the Analysis of Impact Loads of Amphibious Aircraft during Landing on the Water. In Proceedings of the IOP Conference Series: Materials Science and Engineering, Chennai, India, 16–17 September 2020; Volume 751, p. 012032.
31. Chen, J.; Xiao, T.; Wang, M.; Lu, Y.; Tong, M. Numerical study of wave effect on aircraft water-landing performance. *Appl. Sci.* **2022**, *12*, 2561. [CrossRef]

Disclaimer/Publisher's Note: The statements, opinions and data contained in all publications are solely those of the individual author(s) and contributor(s) and not of MDPI and/or the editor(s). MDPI and/or the editor(s) disclaim responsibility for any injury to people or property resulting from any ideas, methods, instructions or products referred to in the content.